



OPEN Effect of intrinsic heat treatment on the microstructure and mechanical properties of Al-Cu alloy fabricated by wire arc directed energy deposition

Bin Yang¹, Xiaodong Li², Shuang Lei¹, Yating Li¹, Xinyuan Jin¹, Guoping Zhao¹✉ & Xianfeng Li¹

Wire arc directed energy deposition (WADED) represents an appealing approach for producing complex, large-scale, and three-dimensional metallic components from metallic wire, guided by computer-aided design models. In the additive manufacturing process, where components are incrementally constructed layer upon layer, the deposited material experiences a recurring series of temperature fluctuations, essentially undergoing reheating cycles. This study harnesses the inherent heat treatment (IHT) mechanism, characterized by these cyclic reheating phenomena, to orchestrate in situ grain growth partial aging, and non-uniform precipitation of intermetallic compounds during the WADED process of Al-Cu alloy. Consequently, following IHT, as the average grain size expanded from 26.1 μm to 40.1 μm , the micro-hardness and tensile capabilities of the as-deposited alloy exhibited a decline. However, by applying a subsequent solution treatment coupled with a 16-hour aging period, the microstructural variations were significantly mitigated, leading to an enhancement in the mechanical properties of the alloy.

Keywords Wire arc directed energy deposition, Intrinsic heat treatment, Aluminum alloy, Microstructure, Mechanical properties

Wire arc directed energy deposition (WADED) has found extensive application in advanced contexts, characterized by large-scale (meter-level) fabrication and intricate metallic structures. This utilization is attributed to its notable characteristics, which encompass a high deposition rate, efficient material utilization, cost-effectiveness in both production and equipment and a high degree of equipment versatility and scalability^{1–5}. WADED components can be directly manufactured using computer-aided design models and metal wire. This process involves the localized injection of metal wire into a molten pool formed by a focused arc through a feed nozzle, adding successive layers to incrementally construct the three-dimensional component⁶.

Within the WADED process, metallic elements are incrementally deposited to a substantial metallic substrate. This substrate not only serves to efficiently dissipate heat generated during the deposition but also provides essential support for the workpiece throughout the fabrication process. As a consequence of the layer additive characteristic in the WADED fabrication process⁷, diverse regions of the deposited materials encounter a complex thermal profile. The thermal histories within the WADED procedure encompass an initial rapid quenching from the liquid state, succeeded by an inherent heat treatment (IHT) involving cyclic reheating characterized by numerous brief temperature spikes approaching values proximate to the melting point⁸. The intricate thermal dynamics in the WADED process give rise to a multifaceted evolution of the microstructure. In particular, the employment of a tightly focused arc for the formation of a swiftly transiting molten pool can yield relatively elevated solidification velocities and cooling rates.

In the past decade, the utilization of aluminum alloys has experienced a significant upsurge in various automotive and portable device applications, primarily due to their favorable combination of low density and high strength⁹. Among heat-treatable and high-strength Al alloys, Al-Cu alloys are notably attractive because

¹State Key Laboratory of Metal Matrix Composites, School of Materials Science & Engineering, Shanghai Jiao Tong University, Shanghai 200240, China. ²Machinery Manufacturing Co., Ltd. of KSEC, Kunming 650236, China. ✉email: zhaogp@sjtu.edu.cn

of their superior creep strength at elevated temperatures¹⁰. Aluminum-copper alloys are a type of precipitation-hardened Al-based alloy, forming multiple metastable phases during the phase decomposition process¹¹. The phase decomposition process of aluminum-copper alloys is commonly concluded as follows: supersaturated solid solution - G.P.(I) - θ'' phase - metastable θ' phase - stable θ phase¹². Besides, the θ' (Al_2Cu) phase, as an important intermetallic compound, significantly influences subsequent mechanical properties based on its growth, size, morphology, and particle size distribution during thermodynamic processes¹³.

The aging temperature of Al-Cu alloy is relatively low (165 °C), leading to a certain degree of IHT frequently occurring during the repetitive melt-cooling deposition process. IHT is notably observed in WADED. Philipp¹⁴ et al. have documented that IHT has the capacity to induce the precipitation of nickel aluminide (NiAl) in Fe-Ni-Al alloy. Zheng¹⁵ et al. conducted a simulation of the thermal dynamics involved in laser deposition using laser-engineered net shaping. Their findings revealed that the deposited material undergoes a pronounced rapid quenching phenomenon in the early stages of deposition, with an exceptionally high cooling rate. Krakhmalev¹⁶ et al. proposed that the temperatures reached through the process of Selective Laser Melting (SLM) were sufficiently able to initiate diffusional transformation in AISI 420 steel.

Until now, there are still few studies on the effect of intrinsic heat treatment on the WADED process of aluminum alloys. Therefore, this paper fabricated thin-walled components of Al-Cu alloy using FS205 (Al-Cu) as the filling wire and systematically investigated the microstructural evolution, phase transformations, and mechanical properties during the WADED process. And heat treatment processes were applied to eliminate the heterogeneous effects caused by IHT.

This paper is organized as follows: Sect. 2 introduces the experimental materials, equipment and methods used. Section 3 shows the experimental results including temperature evolution, phase composition, microstructure and mechanical properties. The effect of IHT on microstructure and mechanical properties is discussed in Sect. 4. The conclusion of this paper is shown in Sect. 5.

Materials and methods

The WADED system in the present research mainly consisted of a six-axis FANUC robot, a Fronius cold metal transfer (CMT) power source, a torch, an external wire feeder and a working platform. The nominal compositions of the commercial ZL205A wire (1.2 mm in diameter) and the deposit are listed in Table 1. The 6061 substrate plate had dimensions of 200 mm×200 mm×20 mm and was washed in alkaline water and dried in air. This was then followed by mechanical cleaning and degreasing using acetone immediately before deposition. As shown in Fig. 1b, the wall with dimensions of 100 mm×155 mm×20 mm was deposited layer by layer along the centerline of the substrates. The use of wall components primarily serves to simplify the deposition process, facilitating a more focused investigation into the effects of intrinsic heat treatment on the material's microstructure. The CMT-ADV mode was applied for building the wall. In the deposition process, mean current (80 A), voltage (11.5 V), torch travel speed (0.5 m/min), wire feed speed (4.3 m/min), inter-layer cooling time (20 s), shielding gas flow rate (25 L/min) of pure argon (99.99%) and contact tip to workpiece distance (15 mm) were all kept constant for the wall sample.

A 45-layer Al-Cu linear wall structure was deposited to study the microstructural evolution and mechanical properties of the as-deposited WADED component and its response to a standard aging heat treatment. The heat treatment applied to the as-deposited wall structure consisted of two steps, which were solution treatment and artificial aging. The samples were ramped in the furnace at 535 °C for 2 h and subsequently quenched into water. Artificial aging treatment was then carried out at 165 °C for 16 h. Wall samples were then cooled down to room temperature in the furnace.

The wall sample's ends (10 mm) were cut off and discarded. The sampling positions of the wall were sectioned as shown in Fig. 1a. Samples for the microstructure analysis and hardness test were taken from the middle part of the wall. The tensile test samples as shown in Fig. 1c were machined to a final surface roughness less than 1.6 μm. Tensile tests were carried out at ambient temperature by an electro-mechanical universal testing machine following the BS EN ISO6892-1:2009 standard. The specimen was loaded with an initial strain rate of 0.001 s⁻¹. Tensile tests were conducted three times at each location (SH1, SH3, etc.), and the average value was taken. Vickers microhardness testing machine (Zwick Roell Z100) was employed with a 10 kg load for 10s for measuring the hardness. The hardness test started 7 mm from the bottom surface of each wall. 40 tests were conducted along the vertical direction, with a 2.5 mm interval between each position. Three tests were performed at each position, and the average value was taken.

Samples were transverse cross-sectioned from the as-deposited wall for microstructure investigation. Scanning electron microscopy (SEM) (NOVA NanoSEM 230) was employed to take images of the microstructure. The SEM specimens were ground with 180, 400, 800, 1200 and 2500 grit SiC papers under flowing water, then

Compositions	Cu	Mn	Cd	Ti	V	Fe	Si	Al
Wire	5.00	0.40	0.29	0.15	0.100	0.100	0.040	Balance
SH1	4.64	0.36	0.21	0.13	0.093	0.088	0.027	Balance
SH3	5.08	0.40	0.23	0.13	0.089	0.082	0.026	Balance
SH5	5.30	0.41	0.25	0.13	0.089	0.085	0.026	Balance
SH7	5.74	0.44	0.27	0.13	0.088	0.084	0.030	Balance
Heat-treated state	5.22	0.40	0.25	0.13	0.090	0.085	0.029	Balance

Table 1. Chemical composition of the ZL205A wire and the WADED Al-Cu wall (wt %).

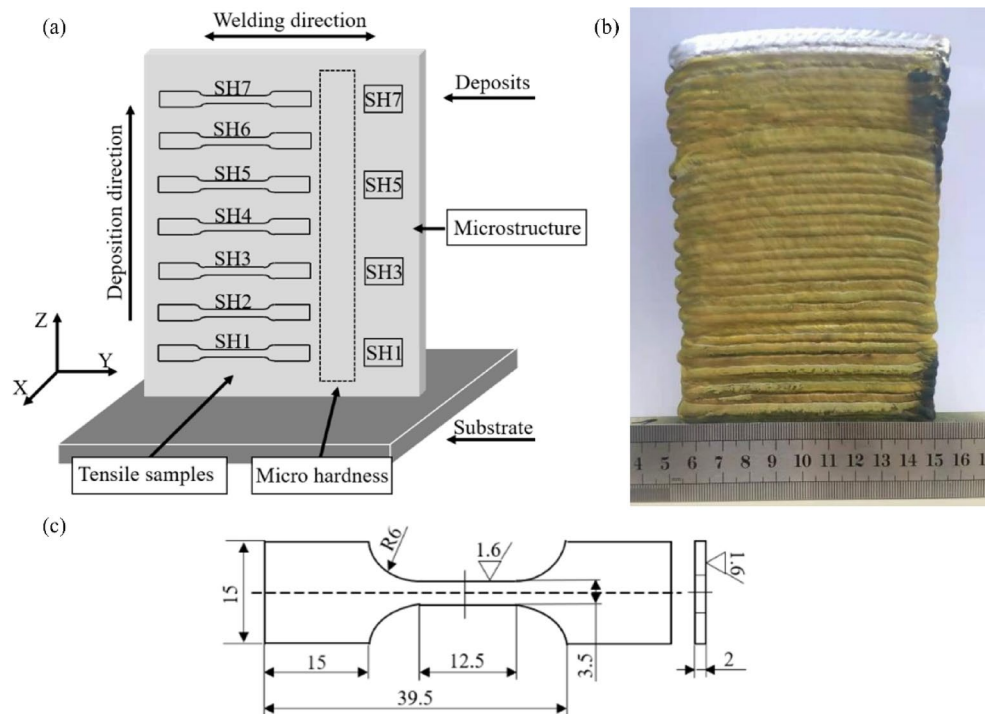


Fig. 1. (a) The sampling positions of the wall; (b) the view of the thin-wall sample; (c) the size of the tensile samples (the figure (a) and (c) were created using PowerPoint software. Version number: LTSC 2021; URL link: <https://software.sjtu.edu.cn/En/List/Office/2021>).

were polished with 5 μm , 1.5 μm and 0.5 μm diamond paste to a mirror finish. Energy dispersive spectrometry (EDS) was used for micro-area composition analysis. Electron back scattered diffraction (EBSD) with a step length of 1.718 μm was carried out for grain size analysis by using the commercial software HKL CHANNEL 5. Fracture surface morphology of the tensile specimens was performed using SEM. The phase constituents near the substrate, at the middle buildup section and top section, were identified using a Rigaku D/max 2500 X-ray diffractometer (XRD) with CuK α radiation ($\lambda=1.5418\text{\AA}$) and a scanning speed of $1^\circ/\text{min}$. The scanning angle (2θ) was set from 20° to 90° and the step size was set at 0.02° . Jade 6 software was used to analyze the XRD patterns. The temperature value of the substrate was measured by a thermometer (LINI-T UT321) after each layer was deposited. Transmission electron microscopy (TEM) (JEM-2100) was used for further characterization of the microstructure. The TEM samples were initially ground on both surfaces using 400, 800, 1200 and 2500 grit SiC papers. Once the sample thickness reached 70–90 μm , discs with a diameter of approximately 3 mm were cut. The samples were then pre-thinned to perforation using a twin-jet electropolishing device, with an electrolyte solution composed of a 3:7 volume ratio of nitric acid to methanol. During the electropolishing process, liquid nitrogen maintained the electrolyte temperature at -30°C . Subsequently, ion thinning was performed on the perforated samples using an ion thinning apparatus for 20 min, at an angle of 3° and a voltage of 3 kV.

Results

Temperature evolution

The WADED process is essentially an additive multi-pass welding process¹⁷. The layer-by-layer additive manufacture is different from the traditional manufacturing process in a unique manner characterized by local melting and directional thermal conduction. In the WADED process, the heat accumulated during deposition is primarily dissipated through thermal radiation and heat transfer to the substrate. The substrate temperature can intuitively reflect the intrinsic heat treatment (IHT) effect on the solidified state at the bottom, resulting from the remelting-solidification process at the top.

Figure 2 shows the temperature evolution of the substrate in the WADED process. The initial temperature of the substrate is 31.2°C . It can be seen the temperature of the substrate ranged from 126°C to 193°C in the layer-by-layer manufacture of the linear wall. The average temperature value is 157.7°C . With the increase of deposited layers, the temperature of the substrate firstly reaches maximum temperature (193°C) at the fifth layer. Then the temperature value of the substrate starts to fluctuate between the sixth layer and the thirtieth layer. From the thirty-first layer, the temperature value gradually decreases from 162.2°C to 136.2°C . It can be seen that the thermal cycling history experienced by SH1-SH7 is different, which will lead to variations in their microstructures. This is because the temperature level (averaging 157.7°C) can induce solid-state phase transformation in the Al-Cu alloy, affecting the microstructure of the solidified layer at the bottom.

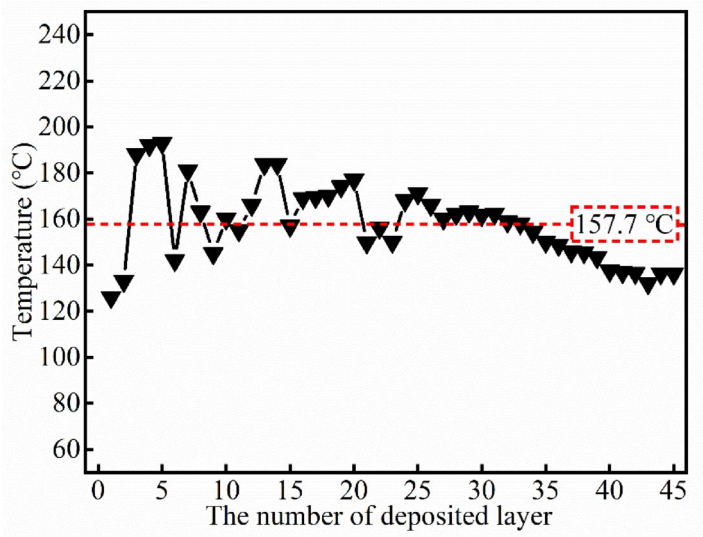


Fig. 2. The temperature of substrate.

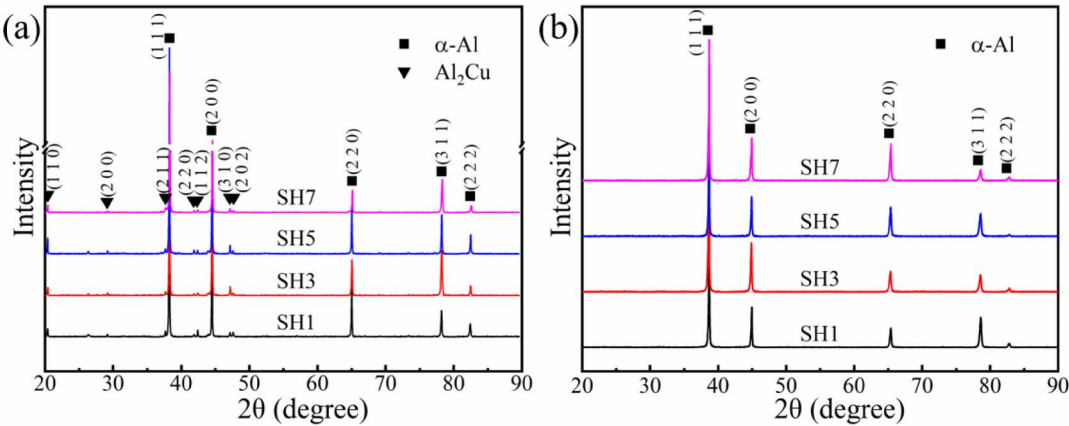


Fig. 3. XRD results of samples extracted from the bottom near the substrate section, middle buildup section and the top near-surface section of the buildup wall: (a) as-deposited condition; (b) heat treatment condition.

Sample	α-Al	Al ₂ Cu
SH1	92.79	7.21
SH3	92.37	7.63
SH5	91.83	8.17
SH7	93.34	6.66

Table 2. Volumetric fraction of the phases in the as-deposited WADED Al-Cu alloy (%).

Phase characterization

Figure 3a presents the XRD results of the as-deposited WADED Al-Cu alloy. It can be seen that the main phase is α-Al. Besides, Al₂Cu also can be confirmed to exist in the four as-deposited components. The top part in the as-deposited condition does not undergo successive thermal cycles, thus only tiny Al₂Cu peaks are observed in the diffractogram. In contrast, more Al₂Cu peaks are found in the middle and bottom parts, indicating a larger amount of Al₂Cu forming. Table 2 summarizes the corresponding Al₂Cu content. From SH1 to SH5, the volume fraction of Al₂Cu gradually increases from 7.21 to 8.17% with the increase in the sample height. However, the top part decreases to 6.66%. After heat treatment, α-Al still existed in the components, while Al₂Cu could not be detected (Fig. 3b).

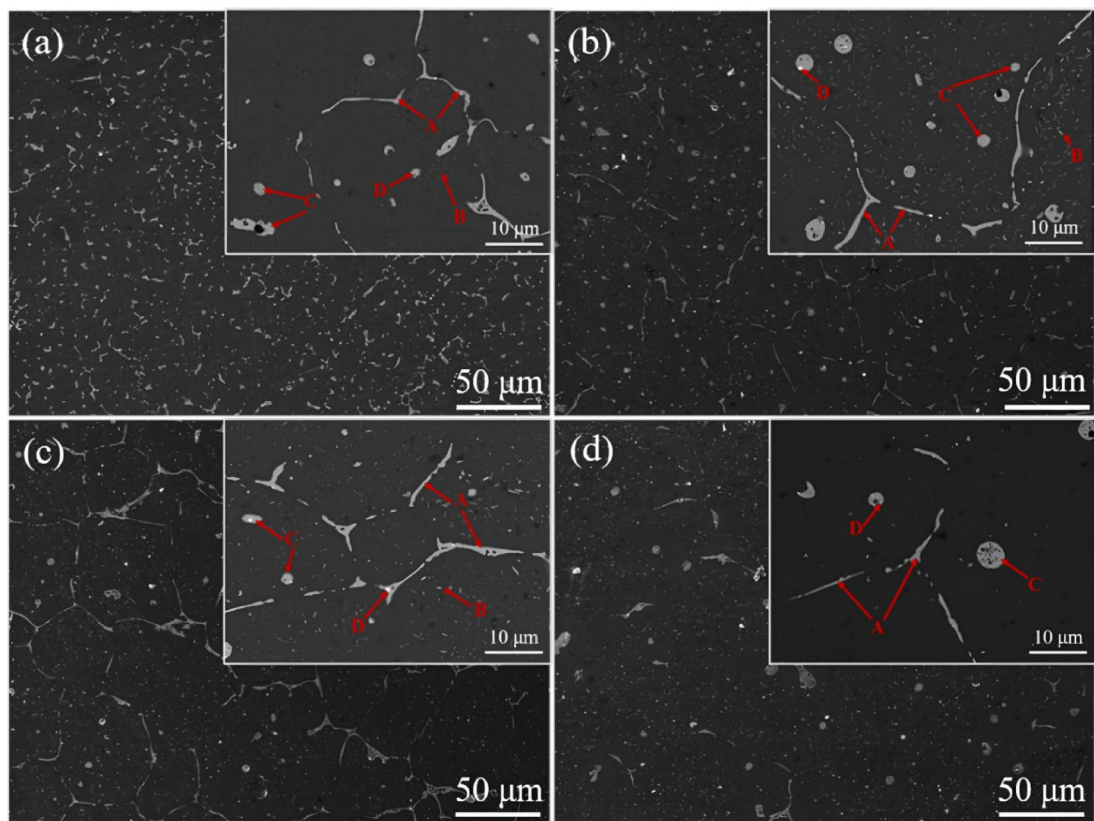


Fig. 4. Microstructure of the as-deposited WADED Al-Cu alloys: (a) SH1; (b) SH3; (c) SH5; (d) SH7.

Points	Al	Cu	Cd	Fe	Mn	Si
A	64.87	35.13	0	0	0	0
B	83.42	16.58	0	0	0	0
C	65.88	24.93	0.35	4.58	3.56	0.70
D	66.23	24.54	0.44	4.78	3.20	0.81

Table 3. Chemical compositions of secondary phases in Fig. 4 (wt%).

Microstructure

The microstructure of the WADED components in the as-deposited condition is shown in Fig. 4. In the bottom part, network-like second-phase particles with light color scatter along as-deposited grain boundaries and dendritic arms, as shown in Fig. 4a. A small number of spherical particles are embedded in intra-grain regions. As shown in Fig. 4b and c, the white network-like eutectic particles scattered along the grain boundaries and similar circular particles distributed in the intra-grain regions in the middle part; whereas the top part (Fig. 4d) contains less network-like eutectic particles and more similar circular particles.

In the WADED process, the as-deposited material undergoes repeated thermal cycles from subsequent depositions and IHT could occur. Table 3 lists the EDS analysis of the secondary phases in Fig. 4. There are four kinds of secondary intermetallic phases in the experimental alloy in Fig. 4, including an irregular grey phase (marked A), a needle-shaped or short rod-like phase (marked B), a circular grey particle (marked C), and a block-like white phase (marked D). The detected EDS data indicated the irregular grey phase (marked A) dominated in grains is θ phase (Al_2Cu). The θ - Al_2Cu particles, in accompaniment with α -Al, connect with each other to establish a network in three-dimensional space (called as eutectic network). It can be seen that a very high area fraction of coarsening θ - $\text{Al}_2\text{Cu}/\alpha$ -Al eutectic network is found with different positions (Fig. 4a–d). Meanwhile, some large cubic particles, needle-shaped particles and small needle-shaped precipitates (marked B) are observed inside the α -Al matrix grains (Fig. 4a–c). Zhang^{18,19} et al. have reported that these needle-shaped particles are θ'' or θ' phase while the large cubic particles are θ - Al_2Cu phase²⁰. Spectrum C and D on the circular phase contain Al, Cu, Fe, Mn, Si and Cd elements. According to the ICP results of the WADED Al-Cu components (4.64–5.74% Cu, 0.36–0.44% Mn), these circular phases contain Al_2Cu phase and $\text{T}(\text{Al}_{20}\text{Cu}_2\text{Mn}_3)$. Moreover, according to ref²¹, the iron-containing phase is $\text{Al}_6(\text{Mn}, \text{Fe})$. These Cu-rich particles easily coarsen and are non-uniformly distributed due to the decreased cooling rate during the repeated thermal cycles of the

WADED process. Besides, this segregation generally causes Cu solute atom depletion zone around the phases, which reduces the mechanical properties²². Further investigation will be undertaken to investigate the influence of those particles on the mechanical properties of this alloy.

Figure 5 illustrates the microstructure of the WADED Al-Cu alloy sample after heat treatment. It can be observed that, following the heat treatment, the majority of the coarse eutectic Al_2Cu phases at the grain boundaries have dissolved and solid-solution into the matrix. The remaining eutectic Al_2Cu phase has transformed into a particulate form. In Al-Cu alloys, apart from Ostwald ripening, the dissolution of eutectic phases formed in the dendritic arms and the oversaturation of hydrogen in the matrix are the primary factors contributing to the significant increase in pore defects in the samples post-heat treatment²³. The dissolution of the eutectic phase during heat treatment generates excess vacancies and voids. At elevated temperatures, when hydrogen atoms are released from dislocations or interfaces, microvoids will heterogeneously nucleate on the surface of the particulate Al_2Cu phase and grow within the voids. Additionally, the number of precipitates at the bottom section is significantly higher than that observed in the middle and top sections.

The TEM results of the WADED Al-5Cu alloy in both the as-deposited and heat-treated states along the [100] axis are presented in Fig. 6. As shown in Fig. 6, two primary types of precipitate phases are identified: the θ' phase and the T phase ($\text{Al}_{20}\text{Cu}_2\text{Mn}_3$). The elongated, perpendicular precipitates correspond to the θ' phase. This phase serves as the primary strengthening phase in the heat-treated samples, as it impedes the motion of dislocations and subgrain boundaries. As a result, the volume fraction of the θ' phase in the heat-treated alloy is considerably higher than that in the as-deposited state. Additionally, the T phase ($\text{Al}_{20}\text{Cu}_2\text{Mn}_3$) precipitates at the tips of the θ' phase and along the grain boundaries. The T phase typically forms during solidification and is primarily located at the grain boundaries²⁴. It acts as a pinning agent, restricting both grain boundary migration and dislocation motion during deformation, thereby contributing to the overall strengthening of the alloy. Moreover, as illustrated in Fig. 6d, the matrix contains substructures that have gradually developed through the accumulation of dislocations. These subgrain boundaries, which are generated by dislocation pile-up, can further hinder the movement of dislocations.

Coloring inverse pole figures (IPF) from cross sections (Y-Z plane) of the as-deposited samples are depicted in Fig. 7. For the WADED process, heat accumulation and thermal cycling induce changes in the microstructure as the different layers are deposited. Fig. 7a–d illustrates that all the grain morphologies are equiaxed and have no evident orientation distribution. The blue region in Fig. 7e–h is the distribution of the grains with a size smaller than 20 μm , and the area ratios are 24.4%, 8.6%, 8.7% and 3.5%, respectively. The grains smaller than 20 μm in the samples SH1 are mostly concentrated at the interlayers, which produces finer grain zones. The grain size is evenly distributed in the middle and top regions, and the concentration phenomenon disappears.

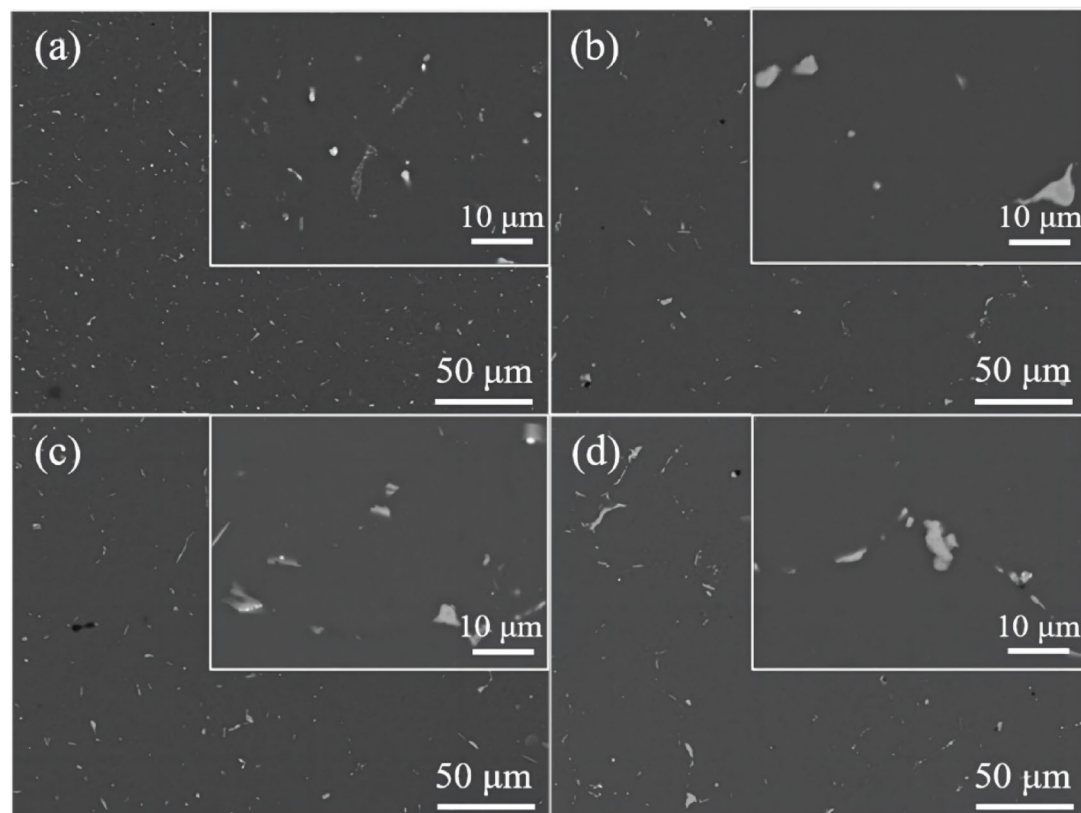


Fig. 5. Microstructure of the heat-treated WADED Al-Cu alloys: (a) SH1; (b) SH3; (c) SH5; (d) SH7.

(a) SH1; (b) SH3; (c) SH5; (d) SH7.

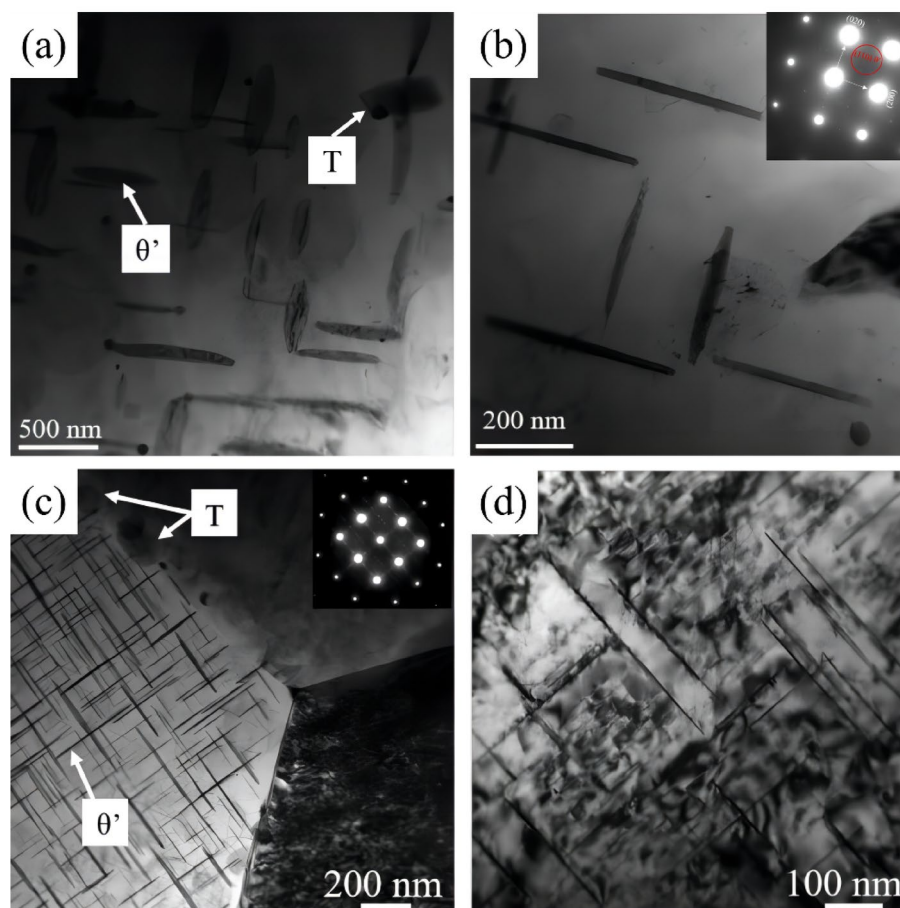


Fig. 6. TEM results of as-deposited (a), (b) and heat-treated (c), (d) WADED Al-Cu alloys in a $[100]_{\text{Al}}$ zone axis.

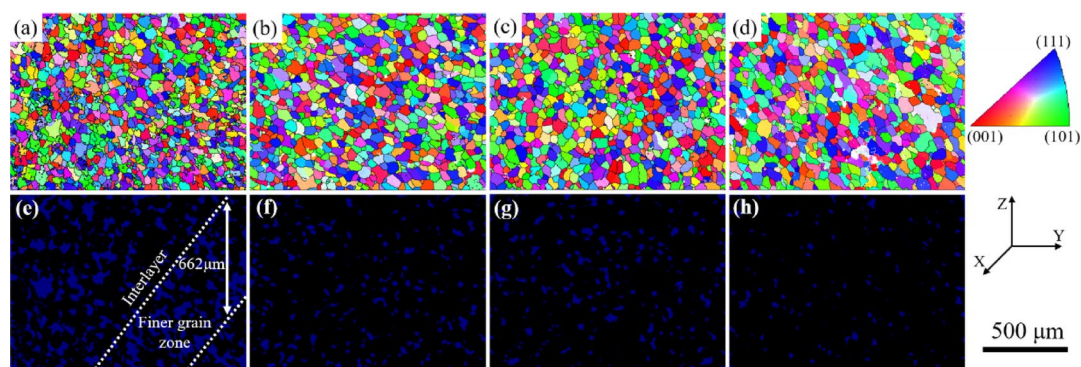


Fig. 7. EBSD results: (a)–(d) inverse pole figure (IPF) map; (e)–(h) grain map with grain size less than $20\text{ }\mu\text{m}$; (a) (e) SH1; (b) (f) SH3; (c) (g) SH5; (d) (h) SH7 (the figures were created using HKL CHANNEL 5 software. Version number: 2019v5.12; URL link: <https://nano.oxinst.cn/products/ebstd/post-processing-software>).

The histograms of grain size distribution for different WADED specimens are shown in Fig. 8. If grain or sub-grain sizes are to be determined from an EBSD map then consideration must be given to the pixel step size about the grain size. According to Humphreys criterion²⁵, 5 pixels (1 in 4) per grain are required to obtain an accuracy of 10%. This means there should be at least 3 pixels in a row within a grain or sub-grain region. Therefore, only grains larger than $5\text{ }\mu\text{m}$ are counted for this research due to the limitation of EBSD scanning resolution. It can be seen that the average grain size increases from $26.1\text{ }\mu\text{m}$ to $40.1\text{ }\mu\text{m}$ as the distance from the wall bottom surface increases from 10 mm to 130 mm, with an increase of 53.6%. This may be caused by

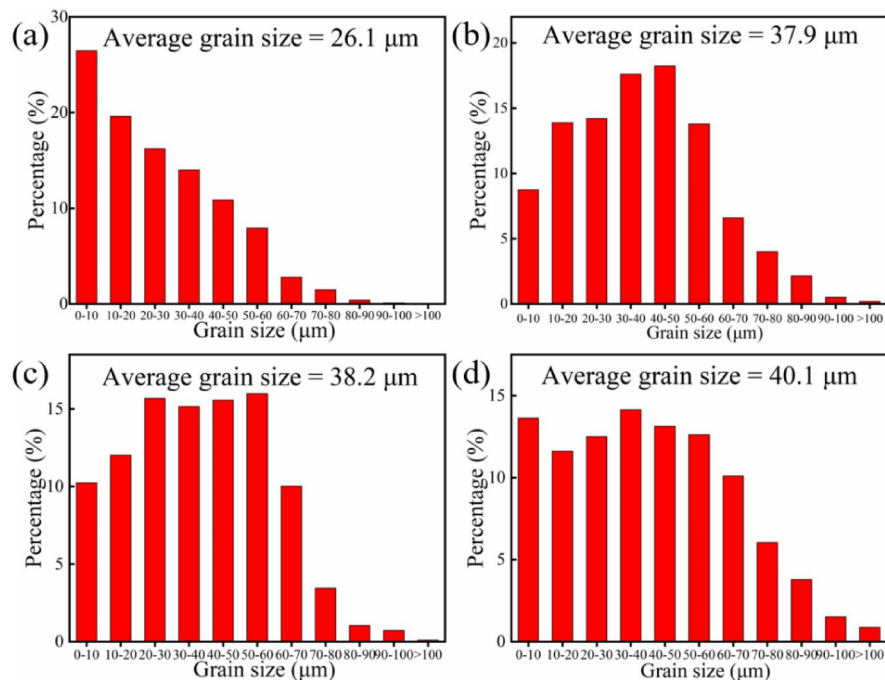


Fig. 8. Grain size distribution for the as-deposited WADED Al-Cu alloy: (a) SH1; (b) SH3; (c) SH5; (d) SH7.

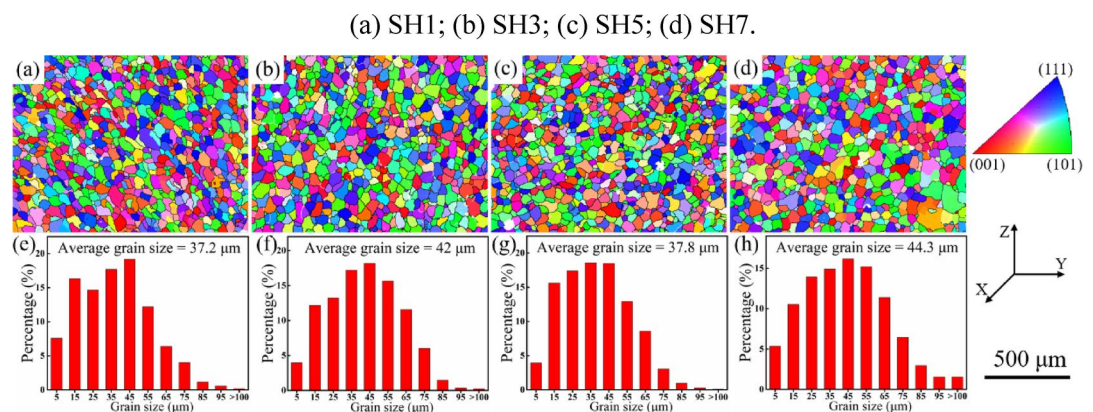


Fig. 9. EBSD results of the heat-treated WADED Al-Cu alloy: (a)–(d) inverse pole figure (IPF) map; (e)–(h) grain size distribution; (a) (e) SH1; (b) (f) SH3; (c) (g) SH5; (d) (h) SH7 (the figures (a)–(d) were created using HKL CHANNEL 5 software. Version number: 2019v5.12; URL link: <https://nano.oxinst.cn/products/ebstd/pos-t-processing-software>. The figures (e)–(h) were created using OriginPro software. Version number: 2019v5.12; URL link: <https://www.originlab.com/OriginProLearning.aspx>).

residual heat from the previous layer. As the previous layer cools down, the dissipation of the heat will effectively provide a preheat for the second layer, decreasing the temperature gradient and creating a cyclic thermal field. The solidification environment promotes the coarsening of some grains in the layer corresponding to samples in the middle and top regions. Furthermore, the average grain size of the samples SH3 and SH5 are 37.9 μm and 38.2 μm , respectively. As shown in Fig. 9, after the heat treatment, the average grain size increases to between 37.2 μm and 44.3 μm and the variation from the bottom to the top layers becomes less pronounced.

Mechanical properties

Figure 10a presents the microhardness variation from the bottom to the top part of the as-deposited Al-Cu alloy. The WADED structure is not uniform in microhardness from the bottom to the top: the material is harder in the bottom part (ranging from 58.5 to 64 HV) but gets softened slightly near and above the bottom part to around 56.9 HV. The difference could be attributed to the different cooling rates between the upper section and the lower section. Combined with the XRD results, it can thus be inferred that Al-Cu alloy produced by WADED is non-uniformly age hardened to different extents from the bottom to the top along the building direction with the

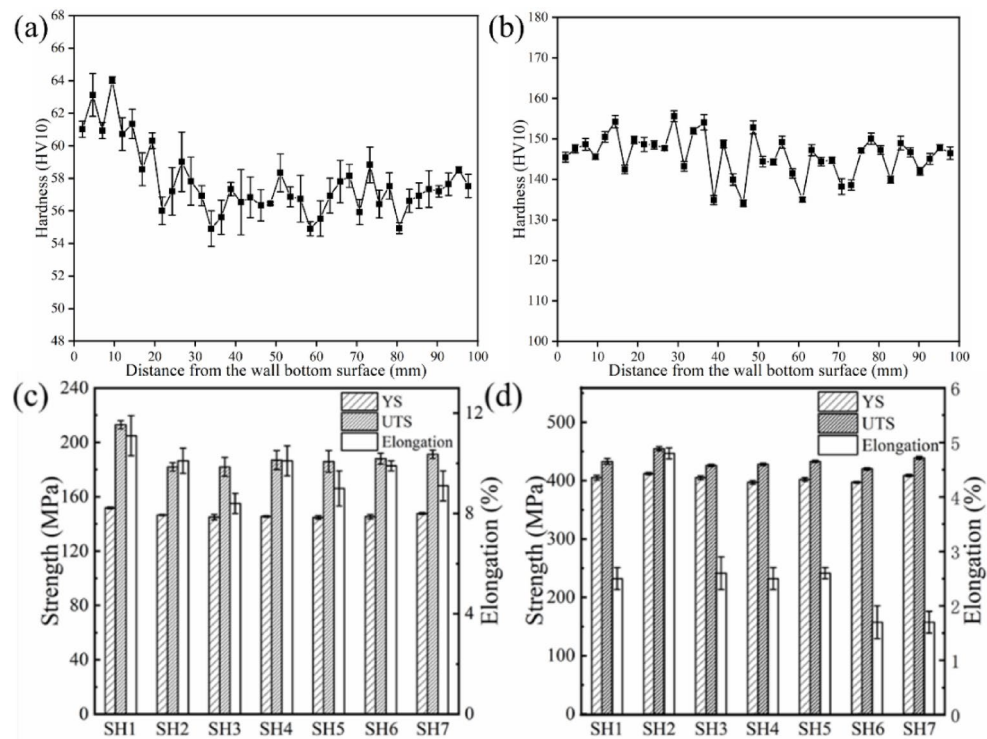


Fig. 10. Mechanical properties: (a,b) the microhardness distribution of the WADED Al-Cu alloy; (c,d) tensile properties for the as-deposited WADED Al-Cu alloys; (a,c) the as-deposited samples, (b,d) the heat-treated samples.

bottom aged more. As shown in Fig. 10b, after heat treatment, the hardness increases to between 134.2 HV and 155.5 HV and the average value is 145.3 HV. The fluctuation of the microhardness value is little, indicating stable microhardness distributing characteristics after heat treatment. The microhardness of WADED Al-Cu alloy can be remarkably improved by solution treatment and the artificial aging process.

The ultimate tensile strength (UTS), yield strength (YS) and elongation (EL) results of WADED-CMT Al-Cu alloys along the building direction with increased distance from the wall bottom surface are shown in Fig. 10c and d. In the as-deposited condition, the UTS, YS and elongation generally reduce from the bottom to the top: from 213 MPa to 191.3 MPa, from 151.7 MPa to 147.7 MPa and from 11.1 to 9.1%, respectively, which is in line with the microhardness measurements and the grain size distribution. After heat treatment, the UTS and YS values at each corresponding location increase noticeably. The UTS increased by 128.2% and the YS increased by 175.4%. The variations in UTS and YS values from the bottom to the top are virtually eliminated. However, there is a significant fluctuation in elongation from the bottom to the top. Compared to the as-deposited state, the elongation of the heat-treated samples has decreased.

Fracture surface

Figure 11 displays the SEM images of the tensile test fractography morphology in the horizontal direction for the WADED Al-Cu alloy. All the fractured surfaces consist of dimples, which are regarded as an indication of ductile fracture. The dimple sizes are different from the specimens with various distances from the bottom surface.

As shown in Fig. 11a, small and deep dimples and cracked second-phase particles can be observed on the fractured surface of the as-deposited Al-Cu alloy. The second phase particles are found embedded at the center of each dimple, which can initiate primary cracks of fracture²¹. Generally, the Cu solute atom depletion zone (SDZ) in the as-deposited alloy is formed around grain boundaries due to the concentrated scattered θ phase particles along the grain boundaries²⁶. These SDZ areas are weaker in strength compared with the other areas. Under static tensile stress, the tearing edges surrounding the particles are generated at these SDZ areas, showing a typical trans-granular fracture mode. Compared with the bottom part of the as-deposited specimen, the dimples of the lower middle part (Fig. 11b) become coarse and the number of the dimples decreases with the increased distance from the bottom surface. The solidification cracks on this surface are responsible for the rupture along the horizontal direction, exhibiting a brittle fracture mode. These cracks may be developed by the inter-grain defects or from the fractured brittle phase particles.

Most of the fracture surface of the middle-upper part (Fig. 11c) and top part (Fig. 11d) is taken by coarse and shallow dimples and micro-voids. These features are typical characteristics of ductile fracture mode. In addition, smooth cleavage planes, cleavage steps and tearing ridges can also be observed, suggesting that cleavage fracture also exists in the specimens of the middle-upper part and top part. Therefore, the fracture transforms from a ductile fracture to a mixture of ductile and cleavage fractures in the middle and top parts.

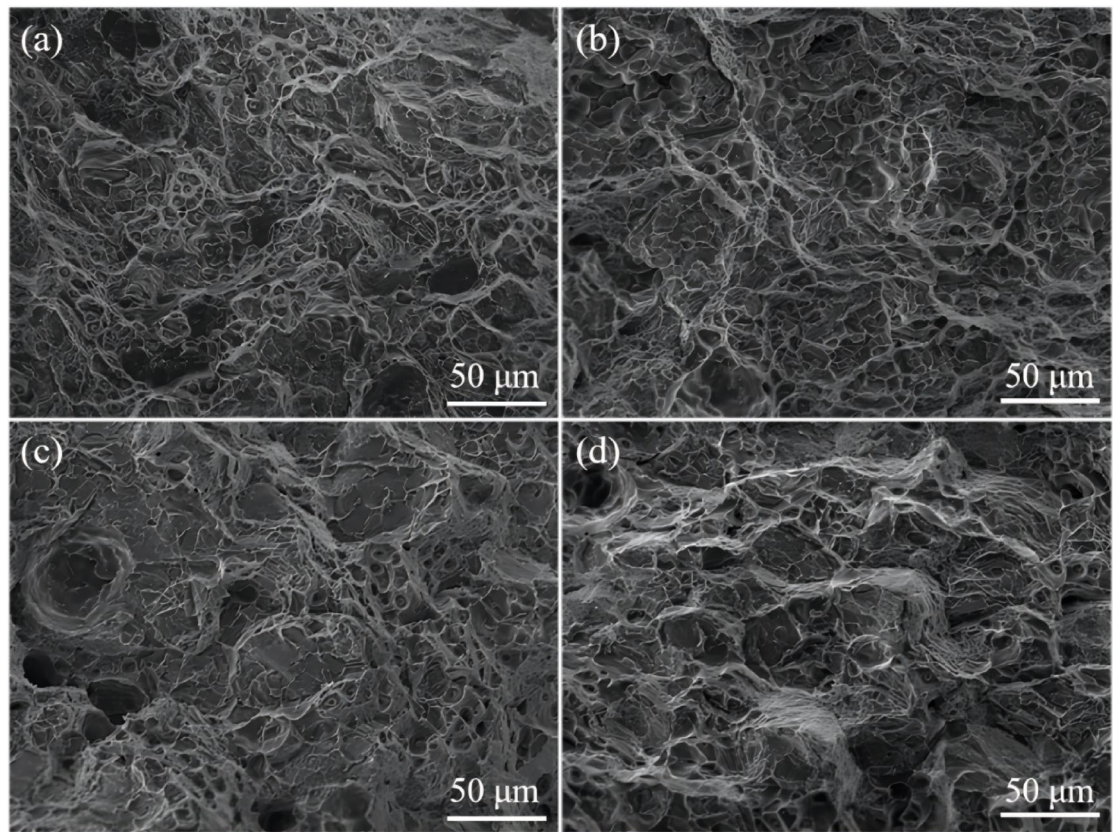


Fig. 11. SEM fractography morphology for tensile specimens of the as-deposited WADED Al-Cu alloys: (a) SH1; (b) SH3; (c) SH5; (d) SH7.

Figure 12 shows the SEM images of the tensile fracture surfaces of heat-treated WAAM-printed Al-Cu alloy samples. From Fig. 12a and c, it can be observed that the fracture surface of the bottom sample contains numerous pores and a few dimples, with second-phase particles present at the bottom of the dimples. Some of these second-phase particles are fractured, and cracks appear in the matrix. After heat treatment of the top sample, as shown in Fig. 12b and d, the tensile fracture surface exhibits a large number of pores, with very few dimples. A significant amount of second-phase particles can be seen along the pore walls and boundaries, and there is evidence of pore wall fragmentation as well as second-phase particle fracture.

Discussion

WADED process and IHT

The layer-by-layer building manner in the WADED process results in heat and mass transfer from the arc, molten wire re-melted a certain amount of the previous layer and the liquid metal solidifies upon it to form a new layer. As shown in Fig. 2, the average temperature value of the substrate is 157.7°C during the WADED process. In the layer-by-layer manufacture of the linear wall, the heat mostly flows from the top layer (where the melt pool is located) to the bottom. Hence, the temperature of the linear wall during the WADED process is higher than the substrate. Since the aging temperature of Al-Cu alloy (165°C) is low, materials are nearly reheated up to such an aging temperature during the whole WADED process. Due to the rapid aging response of Al-Cu alloy, the accumulation of such durations will result in an IHT, which results in all the differences in microstructure evolution and mechanical properties with increased distance from the wall bottom surface.

Effect of IHT on microstructure in the WADED process

According to the solidification principle, the actual liquid temperature is below the liquidus temperature at the solid/liquid interface, which will generate supercooling and a mushy zone. At a high degree of supercooling, the mushy zone becomes so wide that it is easier for the equiaxed dendrites to nucleate than for the columnar dendrites to stretch. A fine grain zone forms finally. The WADED interlayer is located in the molten pool boundary, and the solidification process is similar to the above process. During each deposition, the upper part of the former layer is re-melted and leaves the equiaxed grains in the former layer partially melted. When solidification occurs, the grain growth direction would be perpendicular to the solid/liquid interface in order to follow the maximum temperature gradient. During the deposition process, the bottom part has the highest degree of supercooling so there are evident interlayer fine-grain zones. In the case of the successive layer depositions where the IHT are enhanced and more heat is transferred to the solid of the former layer, which decreases the temperature gradients on the solid/liquid interface and the degree of supercooling, so the fine grain zone disappears and the

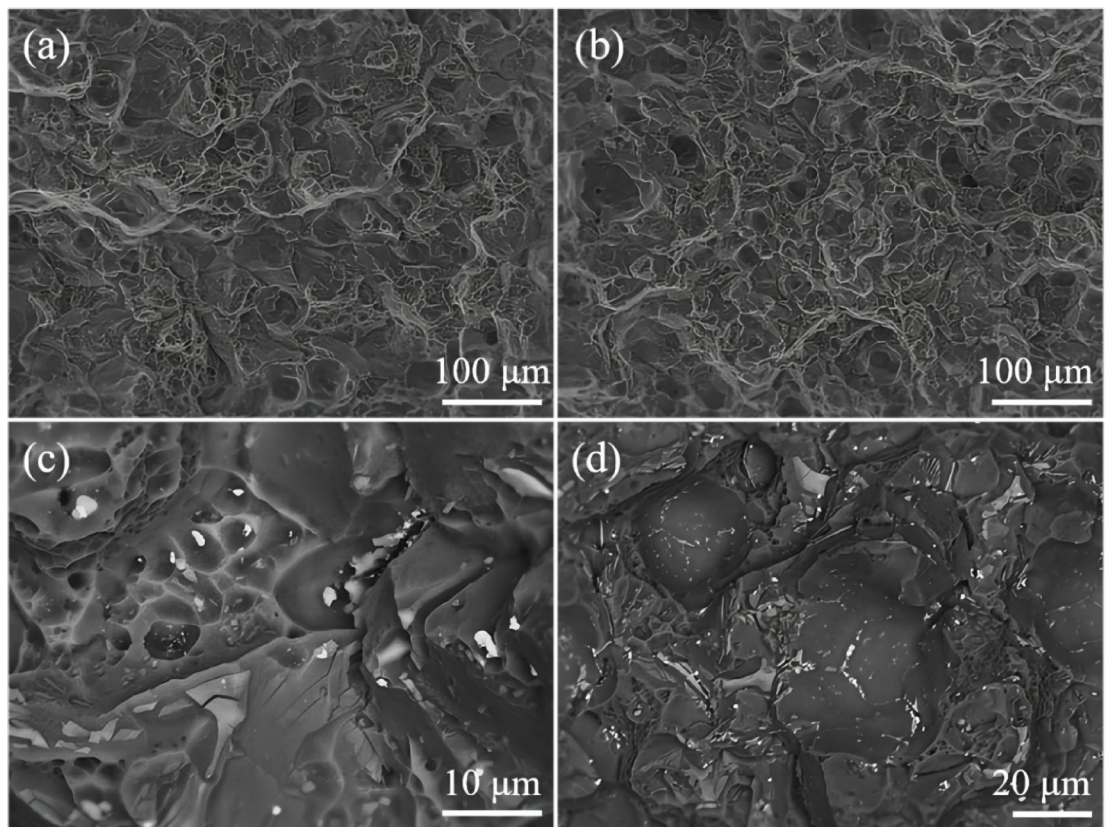


Fig. 12. SEM fractography morphology for tensile specimens of the heat-treated WADED Al-Cu alloys: (a,c) SH1; (b,d) SH7.

average grain size gradually increases with the increased distance from the wall bottom surface. Furthermore, the IHT facilitates the diffusion, solute atoms diffuse out from the unit cell and form precipitates. Different parts undergo a different number of thermal cycles in the WADED process and will have different amounts of intermetallic compounds precipitated: the more thermal cycles, the more precipitates.

Combined with the XRD results, the SEM and EDS of the deposits with different distances from the bottom surface show that the precipitated phases are mainly the massive Al_2Cu phases. In Al-Cu alloy, the number of eutectic structures combined with Scheil's law can be calculated from Eq. (1)²⁷:

$$f_s = (C_e C_1^{-1}) / (1 - k_0) \quad (1)$$

Among them, C_e represents the content of Cu in the eutectic structure, and its value is 0.54 for Al_2Cu ; C_1 is the mass fraction of Cu in the alloy, its value is 0.05, and k_0 is the equilibrium distribution coefficient of the Cu element, taking the value of 0.17²⁸.

From Eq. (1), it can be seen that the content of the eutectic phase increases with the mass fraction of Cu. According to the results in Table 1, during the WAAM process, the mass fraction of Cu increases with the number of deposited layers, leading to a gradual increase in the volume fraction of the eutectic Al_2Cu phase, which is consistent with the XRD results. For SH7, due to its position at the top of the sample, the cooling rate is rapid, and there is no IHT from subsequent deposition layers, which does not meet the premise for the validity of this formula. Therefore, the mass fraction of Cu and the volume fraction of the eutectic Al_2Cu phase in SH7 do not follow this rule. In addition, it can be seen from Fig. 4 that IHT has a greater effect on the morphology and distribution of the Al_2Cu phases. As the number of thermal cycles increases, the precipitated Al_2Cu phases in the grain gradually increase, and their number on the grain boundaries increases. After heat treatment, the coarse eutectic phases dissolve, and solute atoms enter into the solid solution. The influence of thermal cycling is almost eliminated.

Effect of IHT on mechanical properties in the WADED process

The microstructures such as grain size, precipitation strengthening phase, and high-density dislocations can hinder dislocation motion and crystal face slip, which is a decisive factor in improving the mechanical properties of metals. The comprehensive analysis of the microstructures shows that the most obvious change of the microstructures with increased distance from the wall bottom surface is the reduction of intermetallic compounds precipitated and grain growth. The decreased mechanical strength is mainly attributed to these two factors. The IHT from the successive deposits heat treats the previously deposited materials during the WADED

process, thus the deposits closer to the bottom underwent numerous cycles of a different magnitude to age more and get harder than the top part.

It is evident that grains greatly grow with continuous subsequent heat input due to the imbalance between the thermodynamic driving forces of the grains and the pinning forces impeding grain boundary migration in the subsequent deposition²⁹. Grain size is one of the most important microstructural factors in controlling the mechanical properties of aluminum alloys³⁰. In this research, grains are defined as fine grains (FG) and coarse grains (CG) according to two diameter scales of <20 µm and >20 µm, respectively. As shown in Fig. 7, the proportion of FG reaches 25.3% in the top part from 46.1% in the bottom part. There is an obvious increase in CG from 53.9 to 74.7% after IHT. Along with increasing transient thermal cycles, FG scales in the lower middle part and middle-upper part continuously decrease to 22.7% and 22.3%, respectively. CG grains take up 77.3% and 77.7% respectively for the lower middle part and middle-upper part. It can be concluded from the above analysis that IHT in the WADED process is bad for grain refinement in Al-Cu alloy. IHT can significantly decrease the FG proportion and increase the CG proportion, which could decrease the strength properties.

This indicates that grain refinement may be the main strengthening mechanism for the WADED Al-Cu alloy because it is well-known that the mechanical properties of a metal are strongly influenced by the grain and sub-grain sizes. The Hall-Petch equation depicts an increase in yield stress (σ_s) with a decrease in grain size (d)^{31,32}:

$$\sigma_s = \sigma_0 + kd^{-1/2} \quad (2)$$

where σ_0 and k are constants determined experimentally.

There are some other presumed strengthening mechanisms for the Al-Cu alloy due to alloying elements addition. Hu et al.³³ pointed out that the addition of Cd in Al-Cu alloys can trap vacancies and extend their effect on the diffusion of Cu in the Al matrix. Moreover, Cd tends to segregate at the interfaces between θ' (Al_2Cu) and α (Al) phases, as well as reduce the interfacial energy and promote the nucleation of the θ' phase³⁴. Consequently, the resistance of dislocation movement is increased and leads to solution strengthening. Xu et al.³⁵ reported that the Mn and Si elements are added to break up brittle and needle-like Fe-rich intermetallics or to transform them into blocks and this significantly improves the mechanical properties³⁶. The dispersed second phases such as θ' (Al_2Cu) normally provide grain boundaries pinning forces in stabilizing the grain structures.

Conclusions

A wall of Al-Cu alloy has been successfully fabricated using wire arc directed energy deposition process and the specific characterization of the buildup material was divided into four regions along the vertical build direction to investigate the material properties as a function of location. In the layer-by-layer manufacture of the linear wall, the heat mostly flows from the top layer (where the melt pool is located) to the bottom, which results in an IHT that results in some extent of diffusion and precipitation to strengthen the material. During the WADED process, the transient thermal cycling from the successive deposits heat treats the previous materials, thus the deposits closer to the bottom underwent numerous thermal cycles of a different magnitude to be aged more.

The bottom part contains mainly fine and equiaxed α -Al grains with Al_2Cu precipitates distributed both inside grains and along grain boundaries. The grain refinement and the existence of Al_2Cu precipitates induced significant fine grain strengthening and solution strengthening respectively in the bottom region. However, the average grain size increases from the bottom part (26.1 µm) to the top part (40.1 µm) to the top part, which is caused by a variation in the specific cooling rate of the deposited layers. From the bottom part to the top part, the microhardness and strength properties are gradually decreased and the fracture transforms from a ductile fracture to a mixture of ductile and cleavage fracture because the average grain size increases and less intermetallic compounds are precipitated, as indicated by EBSD grain size measurements and XRD phase statistics results. Furthermore, the major strengthening mechanism of the as-deposited WADED Al-Cu alloy is fine grain strengthening and solution strengthening.

Solution and aging heat treatment have been applied to WADED Al-Cu alloy, which eliminates the microstructural heterogeneity from the bottom to the top and gives an increase of 128.2% in UTS and 175.4% in YS.

Data availability

Data is provided within the manuscript. And if someone wants to request the data from this study, please contact with the corresponding author (Guoping Zhao, zhaogp@sjtu.edu.cn).

Received: 26 September 2024; Accepted: 21 April 2025

Published online: 16 May 2025

References

- Gu, J. et al. Microstructure, defects, and mechanical properties of wire + arc additively manufactured Al-4.3Cu-1.5Mg alloy. *Mater. Des.* **186**, 108357. <https://doi.org/10.1016/j.matdes.2019.108357> (2020).
- Zhao, X. et al. Microstructure evolution and properties of novel AZ31B/SiCps composites prepared based on wire-arc directed energy deposition. *J. Mater. Res. Technol.* **25**, 698–713. <https://doi.org/10.1016/j.jmrt.2023.05.262> (2023).
- Zhu, Z. et al. Recent progress on the additive manufacturing of aluminum alloys and aluminum matrix composites: microstructure, properties, and applications. *Int. J. Mach. Tools Manuf.* **190**, 104047. <https://doi.org/10.1016/j.ijmachtools.2023.104047> (2023).
- Zhao, X. et al. Microstructure and mechanical properties of 304 stainless steel produced by interpass milling hybrid direct energy deposition-arc. *J. Mater. Res. Technol.* **27**, 3744–3756. <https://doi.org/10.1016/j.jmrt.2023.10.137> (2023).
- Horgar, A. et al. Additive manufacturing using WAAM with AA5183 wire. *J. Mater. Proc. Technol.* **259**, 68–74. <https://doi.org/10.1016/j.jmatprotec.2018.04.014> (2018).

6. Yehorov, Y., João da Silva, L. & Scotti, A. Balancing WAAM production costs and wall surface quality through parameter selection: a case study of an Al-Mg5 alloy multilayer-non-oscillated single pass wall. *J. Manuf. Process.* **3**, 32. <https://doi.org/10.3390/jmmp3020032> (2019).
7. Sun, R. et al. Microstructure, residual stress and tensile properties control of wire arc additive manufactured 2319 aluminum alloy with laser shock peening. *J. Alloy Compd.* **747**, 255–265. <https://doi.org/10.1016/j.jallcom.2018.02.353> (2018).
8. Xu, X. et al. Microstructural evolution and mechanical properties of Maraging steel produced by wire + arc additive manufacture process. *Mater. Charact.* **143**, 152–162. <https://doi.org/10.1016/j.matchar.2017.12.002> (2018).
9. Ma, P., Liu, C., Wu, C., Liu, L. & Chen, J. Mechanical properties enhanced by deformation-modified precipitation of θ' -phase approximants in an Al-Cu alloy. *Mater. Sci. Eng. A* **676**, 138–145. <https://doi.org/10.1016/j.msea.2016.08.068> (2016).
10. Hutchinson, C., Fan, X., Pennycook, S. & Shiflet, G. On the origin of the high coarsening resistance of plates in Al-Cu-Mg-Ag alloys. *Acta Mater.* **49**, 2827–2841. [https://doi.org/10.1016/S1359-6454\(01\)00155-0](https://doi.org/10.1016/S1359-6454(01)00155-0) (2001).
11. Takeda, M. et al. Discontinuity of G.P. (I) zone and Θ' phase in an Al-Cu alloy. *Scripta Mater.* **41**, 643–649. [https://doi.org/10.1016/S1359-6462\(99\)00137-2](https://doi.org/10.1016/S1359-6462(99)00137-2) (1999).
12. Biswas, A., Siegel, D. J., Wolverton, C. & Seidman, D. Precipitates in Al-Cu alloys revisited: Atom-probe tomographic experiments and first-principles calculations of compositional evolution and interfacial segregation. *Acta Mater.* **59**, 6187–6204. <https://doi.org/10.1016/j.actamat.2011.06.036> (2011).
13. Tian, J., Zhao, Y., Hou, H. & Han, P. D. First-principles investigation of the structural, mechanical and thermodynamic properties of Al₂Cu phase under various pressure and temperature conditions. *Solid State Commun.* **268**, 44–50. <https://doi.org/10.1016/j.ssc.2017.09.016> (2017).
14. Kürsteiner, P. et al. Massive nanoprecipitation in an Fe-19Ni-xAl Maraging steel triggered by the intrinsic heat treatment during laser metal deposition. *Acta Mater.* **129**, 52–60. <https://doi.org/10.1016/j.actamat.2017.02.069> (2017).
15. Zheng, B., Zhou, Y., Smugeresky, J., Schoenung, J. & Lavernia, E. Thermal behavior and microstructural evolution during laser deposition with laser-engineered net shaping: part I. Numerical calculations. *Metall. Mater. Trans. A* **39**, 2228–2236. <https://doi.org/10.1007/s11661-008-9557-7> (2008).
16. Krakhmalev, P., Yadroitsava, I., Fredriksson, G. & Yadroitsev, I. In situ heat treatment in selective laser melted martensitic AISI 420 stainless steels. *Mater. Des.* **87**, 380–385. <https://doi.org/10.1016/j.matdes.2015.08.045> (2015).
17. Shen, C., Pan, Z., Cuiuri, D., Dong, B. & Li, H. In-depth study of the mechanical properties for Fe₃Al based iron aluminide fabricated using the wire-arc additive manufacturing process. *Mater. Sci. Eng. A* **669**, 118–126. <https://doi.org/10.1016/j.msea.2016.05.047> (2016).
18. Zhang, Y., Li, R., Chen, P., Li, X. & Liu, Z. Microstructural evolution of Al₂Cu phase and mechanical properties of the large-scale al alloy components under different consecutive manufacturing processes. *J. Alloy Compd.* **808**, 151634. <https://doi.org/10.1016/j.jallcom.2019.07.346> (2019).
19. Zhang, L., Li, R., Jing, R., Zhang, L. & Li, X. A comparative study on the effect of four-source ultrasonic power on the microstructure and mechanical properties of large-scale 2219 aluminum ingots. *J. Occup. Med.* **71**, 2063–2071. <https://doi.org/10.1007/s11837-019-03459-y> (2019).
20. Lombardi, A., Sediako, D., Ravindran, C. & Barati, M. Analysis of precipitation, dissolution and incipient melting of Al₂Cu in B206 al alloy using in-situ neutron diffraction. *J. Alloy Compd.* **784**, 1017–1025. <https://doi.org/10.1016/j.jallcom.2019.01.104> (2019).
21. Gu, J. et al. The strengthening effect of inter-layer cold working and post-deposition heat treatment on the additively manufactured Al-6.3Cu alloy. *Mater. Sci. Eng. A* **651**, 18–26. <https://doi.org/10.1016/j.msea.2015.10.101> (2016).
22. Humphreys, F. Review grain and subgrain characterisation by electron backscatter diffraction. *J. Mater. Sci.* **16**, 3833–3854. <https://doi.org/10.1023/A:1017973432592> (2001).
23. Gu, J. et al. Micropore evolution in additively manufactured aluminum alloys under heat treatment and inter-layer rolling. *Mater. Des.* **168**, 108288. <https://doi.org/10.1016/j.matdes.2019.108288> (2020).
24. Liao, H. et al. Dispersoid particles precipitated during the solution course of Al-12wt%Si-4wt%Cu-1.2wt%Mn alloy and their influence on high temperature strength. *Mater. Sci. Eng. A* **699**, 201–209. <https://doi.org/10.1016/j.msea.2017.04.091> (2017).
25. Sharma, V., Sree, K. K., Nageswara, R. B. & Pathak, S. Effect of microstructure and strength on the fracture behavior of AA2219 alloy. *Mater. Sci. Eng. A* **502**, 45–53. <https://doi.org/10.1016/j.msea.2008.11.024> (2009).
26. Huang, C. & Kou, S. Partially melted zone in aluminum welds: solute segregation and mechanical behavior. *Weld. J.* **80**, 9–17 (2001).
27. Grong, O. *Metallurgical Modelling of Welding* (Institute of Materials, 1997).
28. Wang, S. et al. Study on microstructural and mechanical properties of an Al-Cu-Sn alloy wall deposited by double-wire arc additive manufacturing process. *Metals* **10**, 79. <https://doi.org/10.3390/ma13010073> (2020).
29. Charit, I., Mishra, R. & Mahoney, M. Multi-sheet structures in 7475 aluminum by friction stir welding in concert with post-weld superplastic forming. *Scripta Mater.* **47**, 631–636. [https://doi.org/10.1016/S1359-6462\(02\)00257-9](https://doi.org/10.1016/S1359-6462(02)00257-9) (2002).
30. Gu, J. et al. Deformation microstructures and strengthening mechanisms for the wire + arc additively manufactured Al-Mg4.5Mn alloy with inter-layer rolling. *Mater. Sci. Eng. A* **712**, 292–301. <https://doi.org/10.1016/j.msea.2017.11.113> (2018).
31. Humphreys, F., Prangnell, P. & Priestner, R. Fine-grained alloys by thermomechanical processing. *Curr. Opin. Solid State Mater. Sci.* **5**, 15–21. [https://doi.org/10.1016/S1359-0286\(00\)00020-6](https://doi.org/10.1016/S1359-0286(00)00020-6) (2001).
32. Dubyna, A., Mogucheva, A. & Kaibyshev, R. Hall-Petch relationship in an Al-Mg-Sc alloy subjected to ECAP. *Adv. Mater. Res.* **922**, 120–125. <https://doi.org/10.4028/www.scientific.net/AMR.922.120> (2014).
33. Hu, Y. et al. A precipitation hardening model for Al-Cu-Cd alloys. *Mater. Des.* **151**, 123–132. <https://doi.org/10.1016/j.matdes.2018.04.057> (2018).
34. Sofyan, B., Raviprasad, K. & Ringer, S. Effects of microalloying with Cd and Ag on the precipitation process of Al-4Cu-0.3Mg (wt%) alloy at 200 °C. *Micron* **32**, 851–856. [https://doi.org/10.1016/S0968-4328\(00\)00093-7](https://doi.org/10.1016/S0968-4328(00)00093-7) (2001).
35. Xu, R. et al. Microstructure evolution and mechanical properties of Al-6.5Cu-0.6Mn-0.5Fe alloys with different Si additions. *T Nonferrous Metal Soc.* **29**, 1583–1591. [https://doi.org/10.1016/S1003-6326\(19\)65065-X](https://doi.org/10.1016/S1003-6326(19)65065-X) (2019).
36. Lin, B. et al. Development of high Fe content squeeze cast 2A16 wrought Al alloys with enhanced mechanical properties at room and elevated temperatures. *Mater. Charact.* **142**, 389–397. <https://doi.org/10.1016/j.matchar.2018.06.009> (2018).

Author contributions

B. Yang: Writing-review & editing. X.D. Li: Investigation. S. Lei: Writing-original draft. Y.T. Li: Investigation. X.Y. Jin: Investigation. G.P. Zhao: Writing-review & editing, Visualization, Data curation. X.F. Li: Conceptualization, Supervision. All authors reviewed the manuscript.

Funding

This research did not receive any specific grant from funding agencies in the public, commercial, or not-for-profit sectors.

Declarations

Ethics approval

The authors confirm that they have abided to the publication ethics and state that this work is original and has not been used for publication anywhere before.

Consent for publication

The authors give consent to the journal regarding the publication of this work.

Consent to participate

The authors are willing to participate in journal promotions and updates.

Competing interests

The authors declare no competing interests.

Additional information

Correspondence and requests for materials should be addressed to G.Z.

Reprints and permissions information is available at www.nature.com/reprints.

Publisher's note Springer Nature remains neutral with regard to jurisdictional claims in published maps and institutional affiliations.

Open Access This article is licensed under a Creative Commons Attribution-NonCommercial-NoDerivatives 4.0 International License, which permits any non-commercial use, sharing, distribution and reproduction in any medium or format, as long as you give appropriate credit to the original author(s) and the source, provide a link to the Creative Commons licence, and indicate if you modified the licensed material. You do not have permission under this licence to share adapted material derived from this article or parts of it. The images or other third party material in this article are included in the article's Creative Commons licence, unless indicated otherwise in a credit line to the material. If material is not included in the article's Creative Commons licence and your intended use is not permitted by statutory regulation or exceeds the permitted use, you will need to obtain permission directly from the copyright holder. To view a copy of this licence, visit <http://creativecommons.org/licenses/by-nc-nd/4.0/>.

© The Author(s) 2025